Revealing the origin of the topological Hall effect in the centrosymmetric shape memory Heusler alloy Mn_2NiGa: A combined experimental and theoretical investigation

Shivani Rastogi,[1] Nisha Shahi,[1] Vishal Kumar,[1] Gaurav K. Shukla,[1] Satadeep Bhattacharjee,[2] and Sanjay Singh[1,*]
[1]*School of Materials Science and Technology, Indian Institute of Technology (Banaras Hindu University), Varanasi 221005, India*
[2]*Indo-Korea Science and Technology Center (IKST), Bangalore 560065, India*

(Received 8 May 2023; revised 9 October 2023; accepted 7 November 2023; published 11 December 2023)

Skyrmions are localized swirling noncoplanar spin textures offering a promising revolution in future spintronic applications. These topologically nontrivial spin textures lead to an additional contribution to the Hall effect, called the topological Hall effect. Here, we investigate the origin of the topological Hall effect—a trademark of skyrmions—in a centrosymmetric shape memory Heusler alloy (SMHA) Mn_2NiGa. The magnetization measurement unveils the presence of austenite to martensite transition in the studied system. The topological Hall effect (THE) in the present system is examined experimentally and theoretically. The presence of a large THE in the austenite (cubic) phase of the system strongly suggests that the observed THE in Mn_2NiGa cannot be attributed to the antiskyrmions stabilized by D_{2d} symmetry as reported earlier. To comprehend the underlying mechanism behind the origin of THE, we have performed micromagnetic simulations for a range of magnetic field with a small value of DMI (local DMI) to consider the possible impact of earlier reported atomic disorder in the centrosymmetric SMHA Mn_2NiGa. The results showed the stabilization of Néel-type skyrmions, which can be assigned to the expected local symmetry breaking at the interface of disorder originated ferromagnetic nanoclusters and ferrimagnetic lattice of the system. A theoretical calculation of topological Hall resistivity by utilizing micromagnetic simulations is performed, which is of the same order as the experimentally obtained values in the both martensite and austenite phases.

DOI: 10.1103/PhysRevB.108.224108

I. INTRODUCTION

Skyrmion, a topologically protected local whirl of spin configuration has revolutionized the spintronics field [1–5]. Skyrmions are potential candidates for information carriers in high-density racetrack memory and other spintronic devices as their topological nature helps them to decouple from crystal lattice and assures skyrmions motion via ultralow-current density [6–8]. The topologically protected skyrmion is quantified by an integer called topological number [9,10]:

$$Q = \frac{1}{4\pi}\int m \cdot (\partial_x m \times \partial_y m)\, dx\, dy, \tag{1}$$

where m is the unit vector in the direction of the magnetization. The topological charge Q associated with the skyrmions can be any integer [11–13]. The Dzyaloshinskii-Moriya interaction (DMI) [14,15] found in noncentrosymmetric magnetic materials is assigned for stabilizing skyrmionic textures [16–19]. The energy associated with this interaction is expressed as $D_{ij} \cdot S_i \times S_j$, where, D_{ij}, S_i, and S_j are DMI vector and spins at ith and jth sites, respectively [14,15]. In general, skyrmions are classified into Bloch, Néel and antiskyrmion [20]. In a Bloch-type skyrmion, spins swirl in the tangential planes, that is, perpendicular to the radial directions on moving from core to periphery, while in the case of Néel-type skyrmion, the spin swirls in radial directions from core to periphery [20–22]. The antiskyrmion, on the other hand, has alternating Bloch and Néel-type moment rotations [23]. Depending on the crystal symmetry of the material, distinct types of skyrmions can be stabilized, viz. C_{nv} symmetry and D_n symmetry with homogeneous DMI ($D_x = D_y$) stabilizes Néel and Bloch skyrmions, respectively [24,25], while D_{2d} symmetry with inhomogeneous DMI ($D_x = -D_y$) stabilizes antiskyrmions [24,26,27].

At first, these swirling-like spin configuration was observed in noncentrosymmetric systems hosting bulk DMI (MnSi [16], $Fe_{1-x}Co_xSi$ [17], Cu_2OSeO_3 [18], MnGe [19]), where the competition between exchange interaction and DMI plays a vital role in the stabilization of these textures [14,15]. This was followed by their exciting emergence in the multilayer thin films with interfacial DMI offering the benefit of material compatibility for direct application in the current spintronic devices [28,29]. In 1963, Arrott theoretically proposed that the imperfections in the ferro/antiferromagnetic materials may cause the breaking of local inversion symmetry at lattice defect sites and result in microstructural-defect-induced DMI (local DMI) in the system, which may give stability to some magnetization states [30]. This was followed by the experimental realization of local DMI in centrosymmetric nanocrystalline terbium (Tb) and holmium (Ho), where vorticity in the magnetization states is reported due to the breaking of local symmetry by intrinsic inhomogeneity [31]. Recently, the stabilization of Néel skyrmions in centrosymmetric Fe_3GeTe_2 due to local symmetry breaking induced by an imbalance of Fe occupancy in the lattice is also reported [32]. The topological Hall effect is considered as a benchmark of skyrmions [33,34]. The interaction of skyrmions

*Corresponding author: ssingh.mst@itbhu.ac.in

with the conduction electrons leads to the generation of a fictitious magnetic field in the real space [34], which is experienced by conduction electrons on passing across a skyrmion. This results in an additional contribution to the measured Hall effect called the topological Hall effect (THE) [34,35]. This exotic phenomenon has been reported in various systems like MnSi [34], Fe_3GeTe_2 [36], Mn_5Si_3 [37], EuAgAs [38], $MnBi_4Te_7$ [39], etc. Besides these, Heusler alloys have emerged as potential candidates for realizing both real-space and momentum-space Berry curvature mediated THE [40]. Heusler alloys are ternary intermetallic compounds offering high electronic and magnetic tunability by interplay with constituent elements [41,42]. The observation of THE associated with the skyrmions has been reported in various Heusler systems like Ni_2MnGa [43], Mn_3Ga [44], Mn_2PtSn [45], Mn_2RhSn [46], etc.

Among above mentioned Heuslers, shape memory Heusler alloy (SMHA) Mn_2NiGa exhibiting ferrimagnetism [47,48], high Curie temperature ($T_C \sim 588$K) [49], room temperature martensitic transformation [49,50], high magnetic field induced strain (MFIS) [49], large magnetocaloric effect (MCE) [51], and spin-valve-like magnetoresistance [52], has gained tremendous attention due to its potential application in magnetic actuators/sensors and spintronic devices [49,52]. Recently, THE was observed in Mn_2NiGa SMHA [53]. The system was reported to be noncentrosymmetric tetragonal Heusler ($I\bar{4}m2$), along with the small cubic phase ($F\bar{4}3m$) at room temperature. The origin of THE in the system was theoretically determined using micromagnetic simulation and attributed to the stabilization of antiskyrmions due to the presence of D_{2d} crystal symmetry in the system [53]. On the other hand, a different study based on neutron diffraction of Mn_2NiGa by Brown *et al.* reported the system to be centrosymmetric ($I4/mmm$) [50]. This study was further supported by another neutron diffraction study where the same system was again reported to be centrosymmetric ($I4/mmm$) with the presence of antisite disorder (13% of Ga sites occupied by Mn_{Ni} atoms) [52]. The antisite disorder resulted in the formation of ferromagnetic (FM) nanoclusters in the ferrimagnetic (FI) lattice where spins are aligned antiparallel to each other [52]. Here, we consider FI as antiferromagnet (AFM). In a recent study, the interfacial DMI is quantitatively measured across an AFM/FM interface [54]. Surprisingly, the calculated interfacial DMI values varying with the antiferromagnetic layer thickness are very small ($<150\,\mu J/m^2$) [54] and close to the earlier reported value of defect-induced DMI ($\sim 450 \pm 70\,\mu J/m^2$) [31]. Thus the ongoing discussion suggests that the observed THE in the centrosymmetric Mn_2NiGa SMHA requires a detailed investigation to understand its origin.

The present manuscript reports a combined experimental and theoretical study of THE in Mn_2NiGa SMHA. The magnetization measurement reveals the structural transition from austenite to the martensite phase. The topological Hall resistivity (THR) measurement shows a relatively larger value in the austenite phase than the martensite phase. The presence of large THE in the austenite (cubic) phase of the system strongly suggests that the observed THE in Mn_2NiGa cannot be assigned to the antiskyrmions stabilized by D_{2d} symmetry as reported earlier [53]. The origin of THE in the present system is then further probed by performing micromagnetic simulations with the small value of DMI (local DMI) to take the earlier reported atomic disorder for the same system into consideration, which resulted in the stabilization of Néel skyrmions. Our findings suggest that the antisite disorder may break the local inversion symmetry at AFM (FI)/FM interface in Mn_2NiGa, which may give rise to interfacial DMI in the local range and thus, Néel skyrmions in the system. Therefore the origin of THE in the SMHA Mn_2NiGa can be accredited to the Néel skyrmions-induced real-space Berry curvature emerged due to atomic disorder present in the system. The theoretical calculation of THE using micromagnetic simulations at distinct magnetic fields, is also performed in the both martensite and austenite phases. The obtained theoretical values are found to be in well-agreement with the experimental THR values.

II. RESULTS AND DISCUSSION

A. Structure, magnetization and resistivity

The ingot of polycrystalline Mn_2NiGa was prepared under an argon atmosphere using the standard arc-melting method [52,55]. The details of sample preparation is provided in Ref. [56]. The profile fitting of room-temperature x-ray diffraction (RT-XRD) pattern of the synthesized sample, exhibiting cubic ($Fm\bar{3}m$) structure, is shown in Fig. S1 of Ref. [56].

The temperature-dependent magnetization *(M(T))* curve at 100 Oe measured for the temperature range of 10 to 380 K is shown in Fig. 1(a). The structural transition temperatures for SMHA Mn_2NiGa is obtained by tangent method [55,57], the zoomed view is shown in the inset of Fig. 1(a). The present sample shows the martensite transition with characteristic temperature (T_{Ms}) $\sim$ 284 K, martensite finish temperature (T_{Mf}) $\sim$ 201 K, austenite start temperature (T_{As}) $\sim$ 250 K and austenite finish temperature (T_{Af}) $\sim$ 327 K, which are close to the values reported earlier in the literature [49,51]. Interestingly, the presence of antiferromagnetic exchange interaction in Mn_2NiGa is indicated by the splitting of zero-field-cooling-warming (ZFCW) and field-cooling (FC) curves as shown in Fig. 1(a) [51,58,59]. The inset of Fig. 1(a) shows the variation of longitudinal resistivity (ρ_{xx}) with temperature during the cooling cycle, which depicts monotonic metallic behavior with a sharp rise around martensitic temperature due to the creation of twins along distinct crystallographic orientations separated by twin boundaries [60].

B. Topological Hall

The Hall resistivity (ρ_{xy}) data taken for a temperature range of 5 to 360 K for the investigation of magneto-transport is shown in Fig. 1(b). The total ρ_{xy} is generally divided into three contributions [40,44]:

$$\rho_{xy} = \rho_{xy}^{O} + \rho_{xy}^{A} + \rho_{xy}^{T}, \tag{2}$$

where ρ_{xy}^{O}, ρ_{xy}^{A}, and ρ_{xy}^{T} denote ordinary, anomalous, and topological Hall resistivity contributions, respectively. The ordinary Hall resistivity is given by $\rho_{xy}^{O} = R_0 H$, where R_0 is the ordinary Hall coefficient. The anomalous Hall resistivity can be written in terms of magnetization (M) and ρ_{xx} as ρ_{xy}^{A}

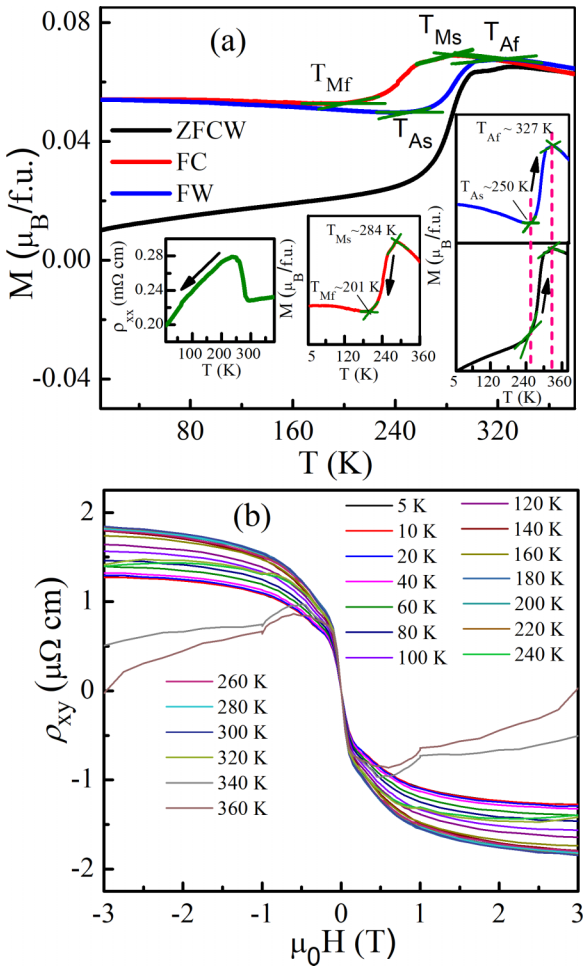

FIG. 1. (a) Temperature-dependent magnetization [$M(T)$] curve at 100 Oe. Inset shows the zoomed view of tangents drawn to determine transition temperatures and zero-field longitudinal resistivity (ρ_{xx}) vs temperature (T) plot for Mn_2NiGa. (b) Field-dependent Hall resistivity (ρ_{xy}) measured at various temperatures.

$= b\rho_{xx}^2 M$, where b is constant [37,44]. It is well known that topological Hall contribution in the Hall resistivity is only found at lower magnetic fields. Therefore the ρ_{xy} data at higher magnetic fields can be simply written as $\rho_{xy} = R_0 H + b\rho_{xx}^2 M$ [44]. This equation is valid for weak magnetic field if $\omega_C \tau \ll 1$, where, $\omega_c = eH/m$ is the cyclotron frequency and $\tau = m/ne^2\rho_{xx}$ is the relaxation time [37]. The values of R_0 and b can be obtained as intercept and slope, respectively, from the linear fitting of $\frac{\rho_{xy}}{H}$ and $\frac{\rho_{xx}^2 M}{H}$ in high field region, which can be further used for ρ_{xy}^O and ρ_{xy}^A calculations [61,62]. The ρ_{xy}^T can then be extracted by subtracting the calculated ρ_{xy}^O and ρ_{xy}^A contributions from the total ρ_{xy} [53] (see Ref. [56] for detailed description). The calculated ρ_{xy}^O and ρ_{xy}^A contributions ($R_0 H + b\rho_{xx}^2 M$) and extracted ρ_{xy}^T from total experimental Hall resistivity (ρ_{xy}) at 5 K (martensite) and 340 K (austenite) are shown in Figs. 2(a) and 2(b), respectively.

The field-dependent ρ_{xy}^T curves for a wide temperature range of 5 to 360 K are shown in Fig. 2(c). The obtained ρ_{xy}^T curve shows the maximum values at $\sim 0.45 \pm 0.15\, T$ for the entire temperature range. It is worth mentioning here that sign of ρ_{xy}^T changes in the martensite phase. This sign reversal is probably associated with the change in net spin polarization of electron states in the martensite phase in comparison to the austenite phase of Mn_2NiGa [48,63,64]. A similar behavior in the ρ_{xy}^T sign, attributed to the change in spin polarization in the martensite phase is also reported in another SMHA Ni_2MnGa [43,65]. It can also be observed from Fig. 2(c) that as the temperature approaches the martensite phase, the value of ρ_{xy}^T decreases drastically. This can be related to the change in structure at the martensite transition [43]. The contour mapping of the magnitude of ρ_{xy}^T with respect to temperature (T) and applied magnetic field ($\mu_0 H$) is shown in Fig. 2(d). The inset of Fig. 2(d) shows the variation of ρ_{xy}^T with temperature where a sharp rise in ρ_{xy}^T value is clearly visible as the temperature approaches the austenite phase.

The unambiguous presence of THE in the austenite (cubic) phase of the centrosymmetric SMHA Mn_2NiGa clearly indicates that the THE in the present system cannot be assigned to the D_{2d} symmetry as reported earlier in the literature [53]. Also, it raises an intriguing question on the type of noncoplanar structures (type of skyrmions/bubbles, etc.) present in the centrosymmetric Mn_2NiGa SMHA. Thus the origin of THE in Mn_2NiGa needs further investigation considering its centrosymmetric structure with the reported antisite disorder, which may cause an emergence of local DMI at AFM (FI)/FM interface. Therefore we have performed micromagnetic simulations at 5 and 300 K considering DMI values expected for local symmetry breaking as earlier reported in the literature [31].

C. Micromagnetic simulation

The details of micromagnetic theory and simulation is provided in Ref. [56] (see also references [4,6,7,12] therein). The energy parameters required to perform micromagnetic simulations such as exchange coefficient (A_{ex}) and anisotropy constant (K), are calculated from experimental $M(H)$ data.

At temperatures much below the transition temperature, demagnetization of ferro- or ferrimagnetic materials often results through the excitation of long-wavelength spin waves, whose energy is quantified by the spin-wave stiffness coefficient (D) [66]. The amplitude of the spin waves is small at low temperatures, and thus, noninteracting spin waves can be used to approximate the excitations close to the ground state. This theory gave rise to Bloch $T^{3/2}$ law, which describes low-temperature magnetization [66,67]. The value of A_{ex} is calculated by first deducing D through fitting the $T^{3/2}$ dependent $M_S(T)/M_S(0)$ data in low-temperature region to the following equation [67,68]:

$$\frac{M_S(T)}{M_S(0)} = 1 - BT^{3/2} \tag{3}$$

and

$$B = 2.612\frac{g\mu_B}{M_S(0)}\left(\frac{k_B}{4\pi D}\right)^{3/2}, \tag{4}$$

where $M_S(T)$, $M_S(0)$, μ_B, g, and k_B are spontaneous magnetization at temperature T, spontaneous magnetization at 0 K, Bohr magneton, Lande's splitting factor, and Boltzmann constant, respectively. The fitting shown in Fig. 3(a) gives

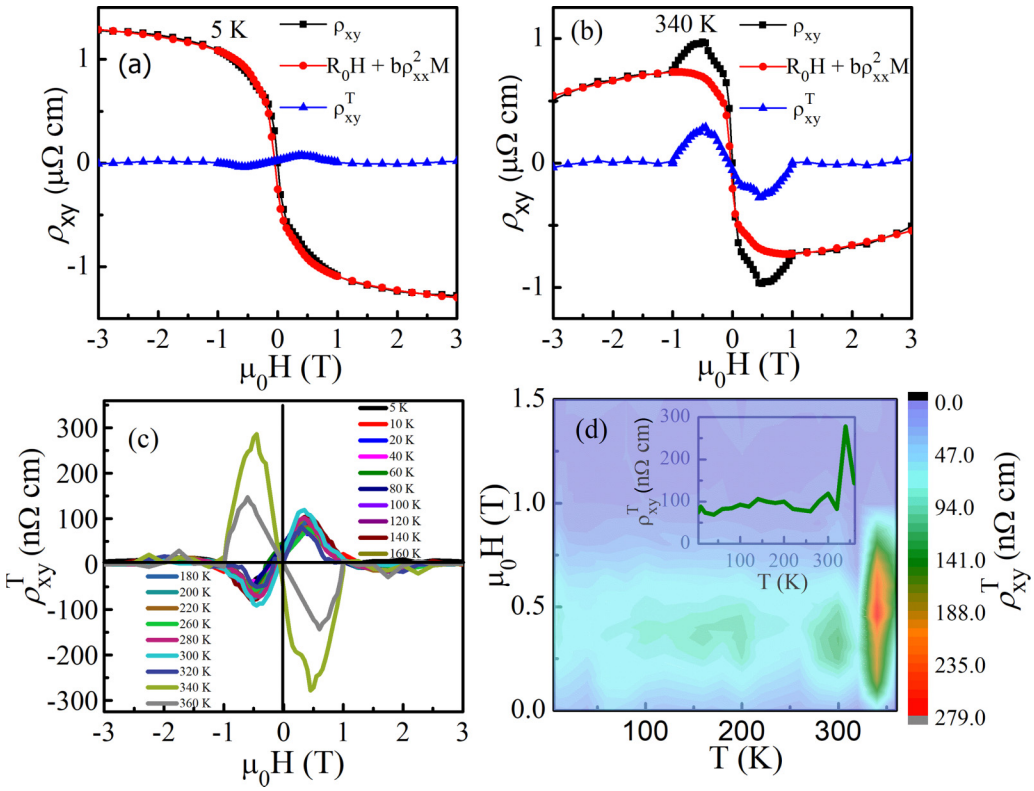

FIG. 2. (a) The Hall resistivity (ρ_{xy}) vs applied magnetic field ($\mu_0 H$(T)) curve (black line), calculated $R_0H + b\rho_{xx}^2M$ curve (red line) and extracted topological Hall resistivity (ρ_{xy}^T) curve (blue) measured at 5 K (martensite). (b) The ρ_{xy} vs $\mu_0 H$(T) curve (black line), calculated $R_0H + b\rho_{xx}^2M$ curve (red line) and extracted ρ_{xy}^T curve (blue) measured at 340 K (austenite). (c) Field-dependent ρ_{xy}^T curves at various temperatures. (d) Contour mapping of the magnitude of ρ_{xy}^T as a function of temperature (T) and $\mu_0 H(T)$. Inset shows the variation of ρ_{xy}^T with temperature.

the value of B and, thus, the value of D is calculated using Eq. (4). The value of A_{ex} can then be determined by using the following relation [69]:

$$D = \frac{2A_{ex}g\mu_B}{M_S}. \tag{5}$$

The values of A_{ex} for 5 and 300 K are calculated to be 3.38×10^{-12} and 2.61×10^{-12} J/m, respectively. The anisotropy constant (K) values to be used in the micromagnetic simulations are deduced from fitting the experimental $M(H)$ data to the Law of approach to saturation [70]:

$$M = M_0\left(1 - \frac{A}{H^2}\right) + \chi H \tag{6}$$

and

$$A = \frac{4}{15}\frac{K^2}{M_0^2}, \tag{7}$$

where M_0, χ, and A are the spontaneous magnetization, high-field susceptibility and a constant which is the function of magnetic anisotropy (K) and M_0 [Eq. (7)], respectively. The anisotropy constant (K) values for 5 and 300 K are calculated to be 6.08×10^4 and 3.79×10^4 J/m^3, respectively, from the fitting of high-field region of $M(H)$ curves [Fig. 3(b)] recorded at respective temperatures. The values of Ms are taken from the experimental M(H) loop (1.74×10^5 A/m at 5 K and 1.34×10^5 A/m at 300 K).

The values of DMI to be used in micromagnetic simulations are taken to be 0.55 mJ/m^2 (300 K) and 0.66 mJ/m^2 (5 K), which is close to the earlier reported local DMI value [31]. The results of micromagnetic simulations obtained at 300 and 5 K for different magnetic fields are shown in Figs. S5 and S6 of Ref. [56], respectively. Initially, the random magnetization state is relaxed for a range of out-of-plane magnetic fields (−3 to 3 T), and the Néel skyrmions are found to be stabilized for the present reported system at lower magnetic fields ($\leqslant -0.4$ to 0.4 T) at both 5 and 300 K. Thus our micromagnetic simulation results suggest that the local symmetry breaking at atomic-disorder induced AFM (FI)/FM interface leads to the origin of interfacial DMI and, thus, stabilizes Néel skyrmions in the system. This gives rise to real-space Berry curvature induced THE in the system.

D. Theoretical calculation of topological Hall

To further ensure the skyrmionic origin of THE, we have calculated the ρ_{xy}^T by first calculating the topological number (Q) of stabilized Néel skyrmionic lattice using a python library [71]. The obtained value of Q for simulated results at various magnetic fields is tabulated in Table I (Ref. [56]). The higher value of Q obtained for 300 K compared to 5 K supports the enhanced experimental ρ_{xy}^T value as the temperature approaches austenite phase. This is followed by the calculation of theoretical ρ_{xy}^T from obtained Q of simulated

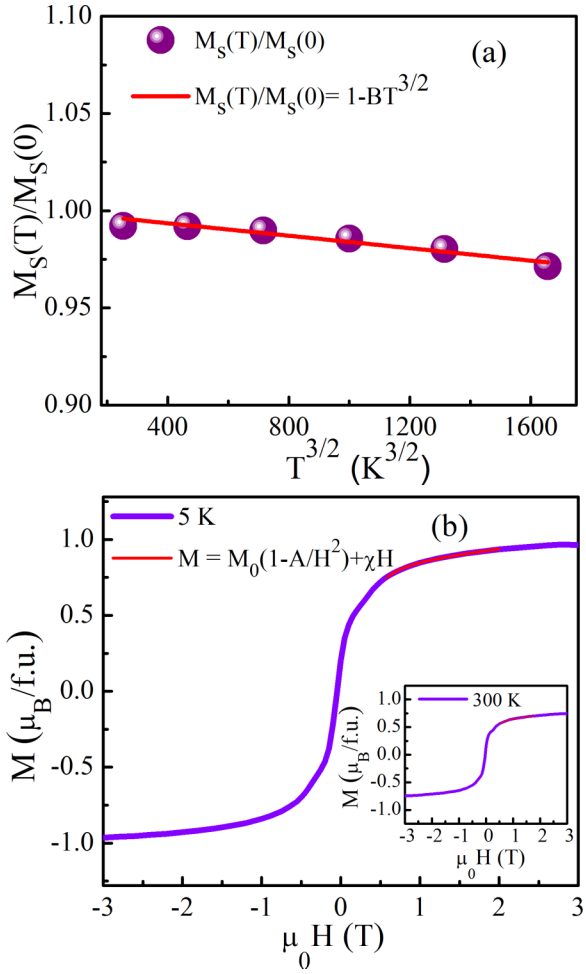

FIG. 3. (a) Fitting of temperature dependence ($T^{3/2}$) of magnetization [$M_S(T)/M_S(0)$] measured at 3 T for Mn_2NiGa. (b) Fitting of the high-field region of [$M(H)$] curve measured at 5 K to Law of approach to saturation. The inset shows the same fitting at 300 K.

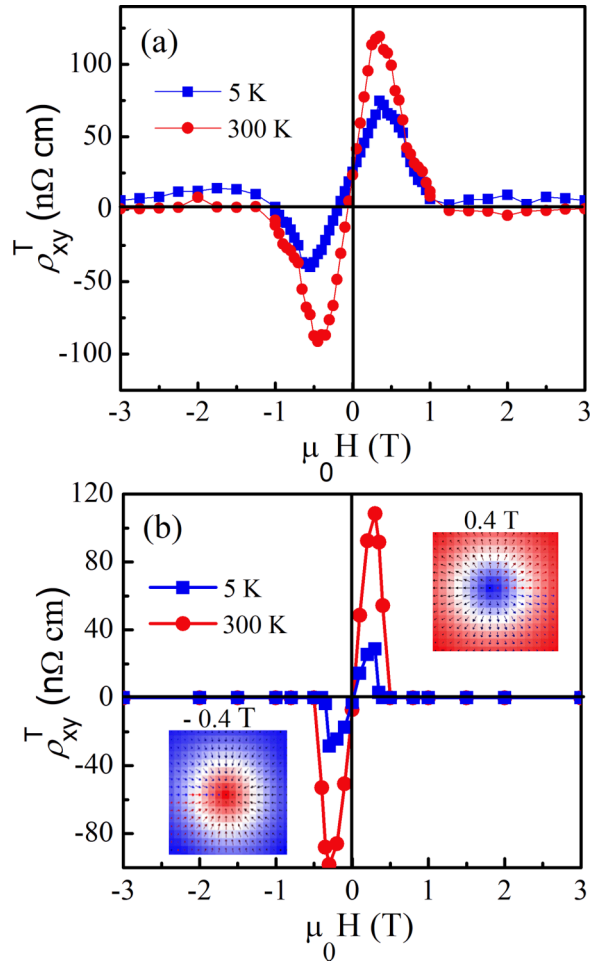

FIG. 4. (a) Experimental topological Hall resistivity (ρ^T_{xy}) curves obtained for 5 and 300 K measured at −3 to 3 T. (b) Theoretical ρ^T_{xy} curves calculated from micromagnetic simulation results obtained for 5 and 300 K. The inset shows the Néel skyrmions obtained at 0.4 and −0.4 T.

skyrmionic lattice at respective magnetic fields by using the following relations [72]:

$$\sigma^T_{xy} = \sigma^0_{xy} \int_S n \cdot (\partial_x n \times \partial_y n)\, dx\, dy, \tag{8}$$

where

$$\sigma^0_{xy} = \sigma_{xx}\left(\frac{e\tau}{2mS}\right)\phi_0 \tag{9}$$

with n, σ^T_{xy}, S, σ_{xx}, τ, and ϕ_0 being the magnetization vector, topological Hall conductivity, surface area of simulation, longitudinal conductivity, scattering time ($\sigma_{xx}m/ne^2$), and flux quantum (h/e), respectively. The term $\int_S n \cdot (\partial_x n \times \partial_y n)\, dx\, dy$ in Eq. (8) is the total flux which is -4π times the topological number (Q) [73,74]. After getting the value of σ^T_{xy} using above Eqs. (8) and (9), the value of ρ^T_{xy} at various magnetic fields can be simply calculated using the following equation [75]:

$$\rho^T_{xy} = \frac{-\sigma^T_{xy}}{\sigma^2_{xx}}. \tag{10}$$

The obtained theoretical ρ^T_{xy} values at 5 and 300 K at different magnetic fields (−3 to 3 T) calculated using the above relations are tabulated in Table I (Ref. [56]). A comparison between experimentally and theoretically obtained ρ^T_{xy} values at 5 and 300 K are shown in Figs. 4(a) and 4(b), respectively. The inset of Fig. 4(b) shows the simulated Néel skyrmions at 0.4 and −0.4 T. The maximum theoretically obtained ρ^T_{xy} values are found to be 27.74 and 108.38 nΩ cm for 5 and 300 K, respectively, which are in the same order as the experimentally obtained values of ρ^T_{xy} (74.74 nΩ cm at 5 K and 119.23 nΩ cm at 300 K). Similarly, the theoretical THE is also calculated at 340 K (austenite phase). The theoretical ρ^T_{xy} value is obtained to be ∼242 nΩ cm, which is comparable to the experimental one (285 nΩ cm). The micromagnetic simulation results obtained for 340 K and a comparison of experimental and theoretical THE at 5, 300, and 340 K is shown in Figs. S7 and S8, respectively, of Ref. [56]. The obtained theoretical THE results were found to remarkably follow the similar trend in magnitude as the experimental THE (see Fig. S8 of Ref. [56]). The comparable theoretical and experimental ρ^T_{xy} values ensure that the origin of THE in the

present system is attributed to the local symmetry breaking at AFM (FI)/FM interface due to atomic disorder present in the system, which resulted in the emergence of interfacial local DMI and, thus, Néel skyrmions in the Mn_2NiGa SMHA.

III. CONCLUSIONS

In summary, the origin of THE in centrosymmetric Mn_2NiGa SMHA is investigated. The magnetization measurement reveals the presence of austenite to martensite transition in the present system. The observation of large THE in the austenite (cubic) phase of the system strongly suggests that the present THE in Mn_2NiGa cannot be accredited to the antiskyrmions stabilized by D_{2d} symmetry as reported earlier [53]. The micromagnetic simulations considering the local DMI resulted in the stabilization of Néel skyrmions, which can be assigned to the local symmetry breaking due to intrinsic disorder present in the SMHA Mn_2NiGa. Thus our work suggests that the Néel skyrmion-induced Real-space Berry curvature is the origin of THE in the present system. This is further validated by calculating the theoretical THE using simulated skyrmionic lattice at 5, 300, and 340 K. The comparable theoretical (27.74 nΩ cm at 5 K, 108.38 nΩ cm at 300 K, and ∼242 nΩ cm at 340 K, respectively) and experimental (74.74 nΩ cm at 5 K, 119.23 nΩ cm at 300 K, and 285 nΩ cm at 340 K) THR values further support our findings. Thus the present study unfolds the ambiguous aspects about the origin of THE in Mn_2NiGa.

ACKNOWLEDGMENTS

S.S. thanks Science and Engineering Research Board of India for financial support through the Core Research Grant (Grant No. CRG/2021/003256) and UGC-DAE CSR for financial support through the "CRS" scheme. S.R. thanks to the PMRF scheme by MHRD, Government of India for financial support. S.S. and S.R. acknowledge UGC-DAE CSR, Indore for providing experimental facility. S.R. thanks Charanpreet Singh for discussion regarding simulation part.

[1] T. H. Skyrme, A unified field theory of mesons and baryons, Nucl. Phys. **31**, 556 (1962).
[2] A. Fert, V. Cros, and J. Sampaio, Skyrmions on the track, Nat. Nanotechnol. **8**, 152 (2013).
[3] N. Nagaosa and Y. Tokura, Topological properties and dynamics of magnetic skyrmions, Nat. Nanotechnol. **8**, 899 (2013).
[4] Y. Tokura and N. Kanazawa, Magnetic skyrmion materials, Chem. Rev. **121**, 2857 (2021).
[5] K. Wang, v Bheemarasetty, J. Duan, S. Zhou, and G. Xiao, Fundamental physics and applications of skyrmions: A review, J. Magn. Magn. Mater. **563**, 169905 (2022).
[6] F. Jonietz, S. Mühlbauer, C. Pfleiderer, A. Neubauer, W. Münzer, A. Bauer, T. Adams, R. Georgii, P. Böni, R. A. Duine, and K. Everschor, Spin transfer torques in MnSi at ultralow current densities, Science **330**, 1648 (2010).
[7] Y. Luo, S. Z. Lin, M. Leroux, N. Wakeham, D. M. Fobes, E. D. Bauer, J. B. Betts, J. D. Thompson, A. Migliori, M. Janoschek, and B. Maiorov, Skyrmion lattice creep at ultra-low current densities, Commun. Mater. **1**, 83 (2020).
[8] X. Z. Yu, N. Kanazawa, W. Z. Zhang, T. Nagai, T. Hara, K. Kimoto, Y. Matsui, Y. Onose, and Y. Tokura, Skyrmion flow near room temperature in an ultralow current density, Nat. Commun. **3**, 988 (2012).
[9] A. Fert, N. Reyren, and V. Cros, Magnetic skyrmions: advances in physics and potential applications, Nat. Rev. Mater. **2**, 17031 (2017).
[10] H. Wu, X. Hu, K. Jing, and X. R. Wang, Size and profile of skyrmions in skyrmion crystals, Commun. Phys. **4**, 210 (2021).
[11] F. N. Rybakov and N. S. Kiselev, Chiral magnetic skyrmions with arbitrary topological charge, Phys. Rev. B **99**, 064437 (2019).
[12] X. Zhang, Y. Zhou, and M. Ezawa, High-topological-number magnetic skyrmions and topologically protected dissipative structure, Phys. Rev. B **93**, 024415 (2016).
[13] D. Foster, C. Kind, P. J. Ackerman, J. S. Tai, M. R. Dennis, and I. I. Smalyukh, Two-dimensional skyrmion bags in liquid crystals and ferromagnets, Nat. Phys. **15**, 655 (2019).
[14] I. Dzyaloshinsky, A thermodynamic theory of "weak" ferromagnetism of antiferromagnetics, J. Phys. Chem. solids **4**, 241 (1958).
[15] T. Moriya, Anisotropic superexchange interaction and weak ferromagnetism, Phys. Rev. **120**, 91 (1960).
[16] S. Mühlbauer, B. Binz, F. Jonietz, C. Pfleiderer, A. Rosch, A. Neubauer, R. Georgii, and P. Böni, Skyrmion lattice in a chiral magnet, Science **323**, 915 (2009).
[17] X. Z. Yu, Y. Onose, N. Kanazawa, J. H. Park, J. H. Han, Y. Matsui, N. Nagaosa, and Y. Tokura, Real-space observation of a two-dimensional skyrmion crystal, Nature **465**, 901 (2010).
[18] T. Adams, A. Chacon, M. Wagner, A. Bauer, G. Brandl, B. Pedersen, H. Berger, P. Lemmens, and C. Pfleiderer, Long-wavelength helimagnetic order and skyrmion lattice phase in Cu_2OSeO_3, Phys. Rev. Lett. **108**, 237204 (2012).
[19] T. Tanigaki, K. Shibata, N. Kanazawa, X. Yu, Y. Onose, H. S. Park, D. Shindo, and Y. Tokura, Real-space observation of short-period cubic lattice of skyrmions in MnGe, Nano Lett. **15**, 5438 (2015).
[20] J. C. Criado, S. Schenk, M. Spannowsky, P. D. Hatton, and L. A. Turnbull, Simulating anti-skyrmions on a lattice, Sci. Rep. **12**, 19179 (2022).
[21] W. Kang, Y. Huang, X. Zhang, Y. Zhou, and W. Zhao, Skyrmion-electronics: An overview and outlook, Proc. IEEE **104**, 2040 (2016).
[22] C. Back, V. Cros, H. Ebert, K. Everschor-Sitte, A. Fert, M. Garst, T. Ma, S. Mankovsky, T. L. Monchesky, M. Mostovoy, N. Nagaosa *et al.*, The 2020 skyrmionics roadmap, J. Phys. D: Appl. Phys **53**, 363001 (2020).
[23] J. Jena, B. Göbel, T. Ma, V. Kumar, R. Saha, I. Mertig, C. Felser, and S. S. Parkin, Elliptical Bloch skyrmion chiral twins in an antiskyrmion system, Nat. Commun. **11**, 1115 (2020).
[24] A. O. Leonov and I. Kézsmárki, Skyrmion robustness in noncentrosymmetric magnets with axial symmetry: The role of anisotropy and tilted magnetic fields, Phys. Rev. B **96**, 214413 (2017).

[25] A. O. Leonov, T. L. Monchesky, N. Romming, A. Kubetzka, A. N. Bogdanov, and R. Wiesendanger, The properties of isolated chiral skyrmions in thin magnetic films, New J. Phys. **18**, 065003 (2016).

[26] M. Hoffmann, B. Zimmermann, G. P. Müller, D. Schürhoff, N. S. Kiselev, C. Melcher, and S. Blügel, Antiskyrmions stabilized at interfaces by anisotropic Dzyaloshinskii-Moriya interactions, Nat. Commun. **8**, 308 (2017).

[27] L. Camosi, N. Rougemaille, O. Fruchart, J. Vogel, and S. Rohart, Micromagnetics of antiskyrmions in ultrathin films, Phys. Rev. B **97**, 134404 (2018).

[28] A. Soumyanarayanan, M. Raju, A. L. Gonzalez Oyarce, A. K. Tan, M. Y. Im, A. P. Petrović, P. Ho, K. H. Khoo, M. Tran, C. K. Gan, and F. Ernult, Tunable room-temperature magnetic skyrmions in Ir/Fe/Co/Pt multilayers, Nat. Mater. **16**, 898 (2017).

[29] H. Y. Kwon, K. M. Song, J. Jeong, A. Y. Lee, S. Y. Park, J. Kim, C. Won, B. C. Min, H. J. Chang, and J. W. Choi, High-density Néel-type magnetic skyrmion phase stabilized at high temperature, NPG Asia Mater. **12**, 86 (2020).

[30] A. Arrott, Dzialoshinski-Moriya interactions about defects in antiferromagnetic and ferromagnetic Materials, J. Appl. Phys. **34**, 1108 (1963).

[31] A. Michels, D. Mettus, I. Titov, A. Malyeyev, M. Bersweiler, P. Bender, I. Peral, R. Birringer, Y. Quan, P. Hautle, and J. Kohlbrecher, Microstructural-defect-induced Dzyaloshinskii-Moriya interaction, Phys. Rev. B **99**, 014416 (2019).

[32] A. Chakraborty, A. K. Srivastava, A. K. Sharma, A. K. Gopi, K. Mohseni, A. Ernst, H. Deniz, B. K. Hazra, S. Das, P. Sessi, and I. Kostanovskiy, Magnetic skyrmions in a thickness tunable 2D ferromagnet from a defect driven Dzyaloshinskii-Moriya interaction, Adv. Mater. **34**, 2108637 (2022).

[33] V. Kumar, N. Kumar, M. Reehuis, J. Gayles, A. S. Sukhanov, A. Hoser, F. Damay, C. Shekhar, P. Adler, and C. Felser, Detection of antiskyrmions by topological Hall effect in Heusler compounds, Phys. Rev. B **101**, 014424 (2020).

[34] A. Neubauer, C. Pfleiderer, B. Binz, A. Rosch, R. Ritz, P. G. Niklowitz, and P. Böni, Topological Hall effect in the A phase of MnSi, Phys. Rev. Lett. **102**, 186602 (2009).

[35] R. Takagi, N. Matsuyama, V. Ukleev, L. Yu, J. S. White, S. Francoual, J. R. Mardegan, S. Hayami, H. Saito, K. Kaneko, K. Ohishi *et al.*, Square and rhombic lattices of magnetic skyrmions in a centrosymmetric binary compound, Nat. Commun. **13**, 1472 (2022).

[36] Y. You, Y. Gong, H. Li, Z. Li, M. Zhu, J. Tang, E. Liu, Y. Yao, G. Xu, F. Xu, and W. Wang, Angular dependence of the topological Hall effect in the uniaxial van der Waals ferromagnet Fe_3GeTe_2, Phys. Rev. B **100**, 134441 (2019).

[37] C. Sürgers, G. Fischer, P. Winkel, and H. V. Löhneysen, Large topological Hall effect in the non-collinear phase of an antiferromagnet, Nat. Commun. **5**, 3400 (2014).

[38] A. Laha, R. Singha, S. Mardanya, B. Singh, A. Agarwal, P. Mandal, and Z. Hossain, Topological Hall effect in the antiferromagnetic Dirac semimetal EuAgAs, Phys. Rev. B **103**, L241112 (2021).

[39] S. Roychowdhury, S. Singh, S. N. Guin, N. Kumar, T. Chakraborty, W. Schnelle, H. Borrmann, C. Shekhar, and C. Felser, Giant topological Hall effect in the noncollinear phase of two-dimensional antiferromagnetic topological insulator $MnBi_4Te_7$, Chem. Mater. **33**, 8343 (2021).

[40] P. Vir, J. Gayles, A. S. Sukhanov, N. Kumar, F. Damay, Y. Sun, J. Kübler, C. Shekhar, and C. Felser, Anisotropic topological Hall effect with real and momentum space Berry curvature in the antiskrymion-hosting Heusler compound $Mn_{1.4}PtSn$, Phys. Rev. B **99**, 140406(R) (2019).

[41] K. Manna, Y. Sun, L. Muechler, J. Kübler, and C. Felser, Heusler, Weyl and Berry, Nat. Rev. Mater. **3**, 244 (2018).

[42] T. Graf, C. Felser, and S. S. Parkin, Simple rules for the understanding of Heusler compounds, Prog. Solid State Chem. **39**, 1 (2011).

[43] A. K. Singh, G. K. Shukla, and S. Singh, Intrinsic anomalous Hall conductivity and real space Berry curvature induced topological Hall effect in Ni_2MnGa magnetic shape memory alloy, J. Phys. D: Appl. Phys. **56**, 044004 (2023).

[44] Z. H. Liu, Y. J. Zhang, G. D. Liu, B. Ding, E. K. Liu, H. M. Jafri, Z. P. Hou, W. H. Wang, X. Q. Ma, and G. H. Wu, Transition from anomalous Hall effect to topological Hall effect in hexagonal non-collinear magnet Mn_3Ga, Sci. Rep. **7**, 515 (2017).

[45] Z. H. Liu, A. Burigu, Y. J. Zhang, H. M. Jafri, X. Q. Ma, E. K. Liu, W. H. Wang, and G. H. Wu, Giant topological Hall effect in tetragonal Heusler alloy Mn_2PtSn, Scr. Mater. **143**, 122 (2018).

[46] K. G. Rana, O. Meshcheriakova, J. Kübler, B. Ernst, J. Karel, R. Hillebrand, E. Pippel, P. Werner, A. K. Nayak, C. Felser, and S. S. Parkin, Observation of topological Hall effect in Mn_2RhSn films, New J. Phys. **18**, 085007 (2016).

[47] S. R. Barman, S. Banik, A. K. Shukla, C. Kamal, and A. Chakrabarti, Martensitic transition, ferrimagnetism and Fermi surface nesting in Mn_2NiGa, Europhys. Lett. **80**, 57002 (2007).

[48] S. R. Barman and A. Chakrabarti, Comment on "Physical and electronic structure and magnetism of Mn_2NiGa: Experiment and density-functional theory calculations", Phys. Rev. B **77**, 176401 (2008).

[49] G. D. Liu, J. L. Chen, Z. H. Liu, X. F. Dai, G. H. Wu, B. Zhang, and X. X. Zhang, Martensitic transformation and shape memory effect in a ferromagnetic shape memory alloy: Mn_2NiGa, Appl. Phys. Lett. **87**, 262504 (2005).

[50] P. J. Brown, T. Kanomata, K. Neumann, K. U. Neumann, B. Ouladdiaf, A. Sheikh, and K. R. Ziebeck, Atomic and magnetic order in the shape memory alloy Mn_2NiGa, J. Phys.: Condens. Matter **22**, 506001 (2010).

[51] S. Singh, S. Esakki Muthu, A. Senyshyn, P. Rajput, E. Suard, S. Arumugam, and S. R. Barman, Inverse magnetocaloric effect in Mn_2NiGa and $Mn_{1.75}Ni_{1.25}Ga$ magnetic shape memory alloys, Appl. Phys. Lett. **104**, 051905 (2014).

[52] S. Singh, R. Rawat, S. E. Muthu, SW D'Souza, E. Suard, A. Senyshyn, S. Banik, P. Rajput, S. Bhardwaj, A. M. Awasthi, and R. Ranjan, Spin-valve-like magnetoresistance in Mn_2NiGa at room temperature, Phys. Rev. Lett. **109**, 246601 (2012).

[53] S. Sen, C. Singh, P. K. Mukharjee, R. Nath, and A. K. Nayak, Observation of the topological Hall effect and signature of room-temperature antiskyrmions in Mn-Ni-Ga D_{2d} Heusler magnets, Phys. Rev. B **99**, 134404 (2019).

[54] X. Ma, G. Yu, S. A. Razavi, S. S. Sasaki, X. Li, K. Hao, S. H. Tolbert, K. L. Wang, and X. Li, Dzyaloshinskii-Moriya interaction across an antiferromagnet-ferromagnet interface, Phys. Rev. Lett. **119**, 027202 (2017).

[55] S. Singh, M. Maniraj, S. W. D'Souza, R. Ranjan, and S. R. Barman, Structural transformations in Mn_2NiGa due to residual stress, Appl. Phys. Lett. **96**, 081904 (2010).

[56] See Supplemental Material at http://link.aps.org/supplemental/10.1103/PhysRevB.108.224108 for details of sample synthesis; room-temperature (RT) x-ray diffraction (XRD) result; description of topological Hall effect (THE) calculation method; details of micromagnetic theory and simulation; micromagnetic simulation results at various temperatures; calculated topological number (Q) and topological Hall resistivity (ρ_{xy}^{T}) at various temperatures and comparison of theoretical and experimental ρ_{xy}^{T} at various temperatures, which includes Refs. [76–79].

[57] D. Xue, R. Yuan, Y. Zhou, D. Xue, T. Lookman, G. Zhang, X. Ding, and J. Sun, Design of high temperature Ti-Pd-Cr shape memory alloys with small thermal hysteresis, Sci. Rep. **6**, 28244 (2016).

[58] T. Krenke, M. Acet, E. F. Wassermann, X. Moya, L. Mañosa, and A. Planes, Ferromagnetism in the austenitic and martensitic states of Ni-Mn-In alloys, Phys. Rev. B **73**, 174413 (2006).

[59] T. Krenke, E. Duman, M. Acet, E. F. Wassermann, X. Moya, L. Mañosa, and A. Planes, Inverse magnetocaloric effect in ferromagnetic Ni-Mn-Sn alloys, Nat. Mater. **4**, 450 (2005).

[60] Z. Nishiyama, *Martensitic Transformation* (Elsevier, New York, 1978).

[61] J. C. Gallagher, K. Y. Meng, J. T. Brangham, H. L. Wang, B. D. Esser, D. W. McComb, and F. Y. Yang, Robust zero-field skyrmion formation in FeGe epitaxial thin films, Phys. Rev. Lett. **118**, 027201 (2017).

[62] S. X. Huang and C. L. Chien, Extended skyrmion phase in epitaxial FeGe (111) thin films, Phys. Rev. Lett. **108**, 267201 (2012).

[63] G. D. Liu, X. F. Dai, S. Y. Yu, Z. Y. Zhu, J. L. Chen, G. H. Wu, H. Zhu, and J. Q. Xiao, Physical and electronic structure and magnetism of Mn_2NiGa: Experiment and density-functional theory calculations, Phys. Rev. B **74**, 054435 (2006).

[64] S. W. D'Souza, T. Roy, S. R. Barman, and A. Chakrabarti, Magnetic properties and electronic structure of Mn-Ni-Ga magnetic shape memory alloys, J. Phys.: Condens. Matter **26**, 506001 (2014).

[65] C. P. Opeil, B. Mihaila, R. K. Schulze, L. Mañosa, A. Planes, W. L. Hults, R. A. Fisher, P. S. Riseborough, P. B. Littlewood, J. L. Smith, and J. C. Lashley, Combined experimental and theoretical investigation of the premartensitic transition in Ni_2MnGa, Phys. Rev. Lett. **100**, 165703 (2008).

[66] K. Mandal, S. Mitra, and P. A. Kumar, Deviation from Bloch $T^{3/2}$ law in ferrite nanoparticles, Europhys. Lett. **75**, 618 (2006).

[67] A. Franco Jr., H. V. Pessoni, and F. L. Machado, Spin-wave stiffness parameter in ferrimagnetic systems: Nanoparticulate powders of (Mg, Zn)Fe_2O_4 mixed ferrites, J. Appl. Phys. **118**, 173904 (2015).

[68] R. Y. Umetsu and T. Kanomata, Spin stiffness constant of half-metallic ferrimagnet in Mn-based Heusler alloys, Phys. Procedia. **75**, 890 (2015).

[69] O. Šipr, S. Mankovsky, and H. Ebert, Spin wave stiffness and exchange stiffness of doped permalloy via *ab initio* calculations, Phys. Rev. B **100**, 024435 (2019).

[70] G. Hadjipanayis, D. J. Sellmyer, and B. Brandt, Rare-earth-rich metallic glasses. I. Magnetic hysteresis, Phys. Rev. B **23**, 3349 (1981).

[71] David Cortés-Ortuño, OOMMF Skyrmion Number (v0.1), Zenodo. https://doi.org/10.5281/zenodo.1296536 (2018).

[72] M. B. Jalil, S. Ghee Tan, K. Eason, and J. F. Kong, Topological Hall conductivity of vortex and skyrmion spin textures, J. Appl. Phys. **115**, 17D107 (2014).

[73] M. Mochizuki, X. Z. Yu, S. Seki, N. Kanazawa, W. Koshibae, J. Zang, M. Mostovoy, Y. Tokura, and N. Nagaosa, Thermally driven ratchet motion of a skyrmion microcrystal and topological magnon Hall effect, Nat. Mater. **13**, 241 (2014).

[74] Y. Liu, G. Yin, J. Zang, J. Shi, and R. K. Lake, Skyrmion creation and annihilation by spin waves, Appl. Phys. Lett. **107**, 152411 (2015).

[75] N. Verma, Z. Addison, and M. Randeria, Unified theory of the anomalous and topological Hall effects with phase space Berry curvatures, Sci. Adv. **8**, eabq2765 (2022).

[76] T. Gilbert, A phenomenological theory of damping in ferromagnetic materials, IEEE Trans. Magn. **40**, 3443 (2004).

[77] X. Zhang, J. Xia, Y. Zhou, X. Liu, H. Zhang, and M. Ezawa, Skyrmion dynamics in a frustrated ferromagnetic film and current-induced helicity locking-unlocking transition, Nat. Commun. **8**, 1717 (2017).

[78] S. Rohart and A. Thiaville, Skyrmion confinement in ultrathin film nanostructures in the presence of Dzyaloshinskii-Moriya interaction, Phys. Rev. B **88**, 184422 (2013).

[79] X. Zhang, G. P. Zhao, H. Fangohr, J. P. Liu, W. X. Xia, J. Xia, and F. J. Morvan, Skyrmion-skyrmion and skyrmion-edge repulsions in skyrmion-based racetrack memory, Sci. Rep. **5**, 7643 (2015).